

First principle studies on the optoelectronic properties of rubidium lead halides

Anupriya Nyayban^{*1}, Subhasis Panda^{†1}, Avijit Chowdhury^{‡1}, and B. Indrajit Sharma^{§2}

¹Department of Physics, National Institute of Technology Silchar, Assam-788010, India

²Department of Physics, Assam University, Silchar-788011, India

Abstract

Entirely inorganic perovskites have attracted enormous attention of late owing to their outstanding applications in optoelectronics including highly stable perovskite solar cells. In-depth understanding of the optoelectronic and transport properties of such materials are vital for practical implementation of the same. The carrier transport properties of the electronic devices based on perovskite materials significantly depend on the effective mass of the respective charge carriers. Here, we have performed first principle calculations with FP-LAPW method for the orthorhombic rubidium lead halide structures (RbPbX₃, where X=I,Br,Cl) to study the optoelectronic and transport properties. The effective mass of electron (hole) is found to be minimum for RbPbBr₃ (RbPbI₃), suggesting an efficient transport of electrons (holes) in the corresponding materials. Our calculated values such as the dielectric constants, refractive indices, absorption coefficients and reflectivities show good agreement with reported experimental data. To the best of our knowledge, ab-initio study of electronic and optical properties of RbPbBr₃ & RbPbCl₃ in orthorhombic phase (NH₄CdCl₃ type structure) is reported for the first time.

1 Introduction

The organic-inorganic halide perovskites have achieved tremendous attention as solar cell materials for the last decade [1–5]. The reasons being their strong absorption to the visible range and ability to transport photo-excited electrons and holes with diffusion length longer than the thickness of the film [6]. The lifetime and effective masses of carries are also high and low respectively for hybrid perovskite. These are required for the material to become an efficient solar cell. The main problem with these hybrid halide perovskites is that they are not thermodynamically stable at ambient conditions. For example, organic-inorganic lead iodide perovskites change to PbI₂ at atmospheric conditions within hours or days [7, 8]. Moreover, the dipole due to the organic cation makes the perovskite structure distorted for the hybrid halide perovskites [9]. These perovskite solar cells (PSC) show current-voltage hysteresis [10], which can reduce the stability in PSC and also affects the power conversion efficiency [11]. These are hindrances to commercialize hybrid halide perovskite solar cells. As the inorganic cation is anisotropic in geometry and less volatile, completely inorganic perovskite solar cell can diminish the hysteresis and hence increases the mobility of electrons [12]. The replacement of A cation in ABX₃

^{*}anupriya@rs.phy.student.nits.ac.in

[†]subhasis@phy.nits.ac.in

[‡]avijit@phy.nits.ac.in

[§]indraofficial@reiffmail.com

type structure is a point of interest due to the fact that the stability comes from the A cation. Therefore many efforts are going on to understand the optoelectronic properties of inorganic perovskites due to its high stability. CsPbX_3 , where $X=\text{I,Br,Cl}$, were found to have comparable solar cell device performance as hybrid perovskite MAPbI_3 while having better stability [13–15]. Halide replacement also influences the absorbance as well as the carrier transportation. The variation of different halide changes the mobility from 3 to 5 cm^2/Vs when carrier concentration varies from 10^{15} to 10^{18} cm^{-3} [16]. CsSnI_3 is also a promising candidate for the optoelectronic devices having a direct band gap of 1.3 eV and mobility of 400 cm^2/Vs [17]. The ionic radii of Cs^+ , Rb^+ are 1.76 and 1.52 Å producing the Goldschmidt’s tolerance factors (t) in case of APbI_3 to be 0.81 and 0.78 respectively [18]. These tolerance values are in the range ($0.7 < t < 1$) of stable halide perovskites. Few studies have been reported on RbPbX_3 structures. A study has been reported on $\text{Rb}_{1-x}\text{Cs}_x\text{PbI}_3$ that while increasing the x content of Cs, there is a decrease in lattice constants, binding energies, band gaps and carriers’ effective masses [19]. The static dielectric constant has been increased when Rb content increases over CsPbI_3 and indicates the increasing solar cell performance. The performance of RbPbI_3 as solar cell was reported in another study with FTO/ TiO_2 / RbPbI_3 /Spiro–MeOTAD/Au configuration [12]. The device was observed to have open circuit voltage as 0.62 V, photo-current density as 3.75 mA/cm^2 , fill factor as 44.60% and power conversion efficiency as 1.04% in the direction of reverse sweeping. It reveals the lower performance of RbPbI_3 as solar cell. Therefore it makes an opportunity to study thoroughly about the optoelectronic properties of RbPbX_3 so that further investigation can be made to find a highly stable perovskite making it suitable for commercial applications.

RbPbI_3 gets the orthorhombic structure of NH_4CdCl_3 in the $Pnma$ space group and does not change to any other phase before it melts [20]. At room temperature, RbPbBr_3 has a mixed phase of RbPbBr_3 of $Pnma$ and RbPb_2Br_5 of $I4/mcm$ space group. The room temperature dominant phase (96.7%) of RbPbBr_3 has the orthorhombic structure of NH_4CdCl_3 type. It undergoes transitions to different phases when it is heated till 350°C. The tetragonal phase of $I4/mcm$ is dominated at 50°C while at 250°C both the room temperature one and a distorted perovskite phase of $Pnma$ space group exist [21]. Like RbPbBr_3 there is a mixture of $\text{Rb}_6\text{Pb}_5\text{Cl}_{16}$ of $P4/mbm$ and RbPb_2Cl_5 of $P2_1/c$ space group at room temperature. But RbPbCl_3 has been found to form a tetragonal phase at 320°C and cubic phase at 350°C with $P4/mbm$ and $Pm\bar{3}m$ space groups respectively [21].

In this study we have reported a comparative study of the optoelectronic properties of RbPbX_3 with the help of first principle calculations. To make a suitable comparison, the stable NH_4CdCl_3 structure of room temperature has been considered for all. The NH_4CdCl_3 type structure for RbPbCl_3 is the hypothetical one.

The computational method is described in Sec.2. Sec. 3 deals with mainly results obtained in this study. The electronic structures of the studied materials are given in sub-section 3.1. The detailed description of optical properties and transport properties are presented in sub-section 3.2 and 3.3 respectively. Finally we summarize our observations and conclude in Sec. 4.

2 Computational method

The present calculations were performed using Wien2k [22] with the FP-LAPW method. Spin orbit coupling (SOC) has been excluded in the entire calculation. Although Wien2k gives the option of including local orbits in the basis and hence improves linearization and proper orthogonality, we have not included the local orbit in the basis set to reduce the computational cost. There is no shape approximation made for potential and the electronic charge density. GGA based exchange correlation potential is treated with the scheme of Perdew, Burke and

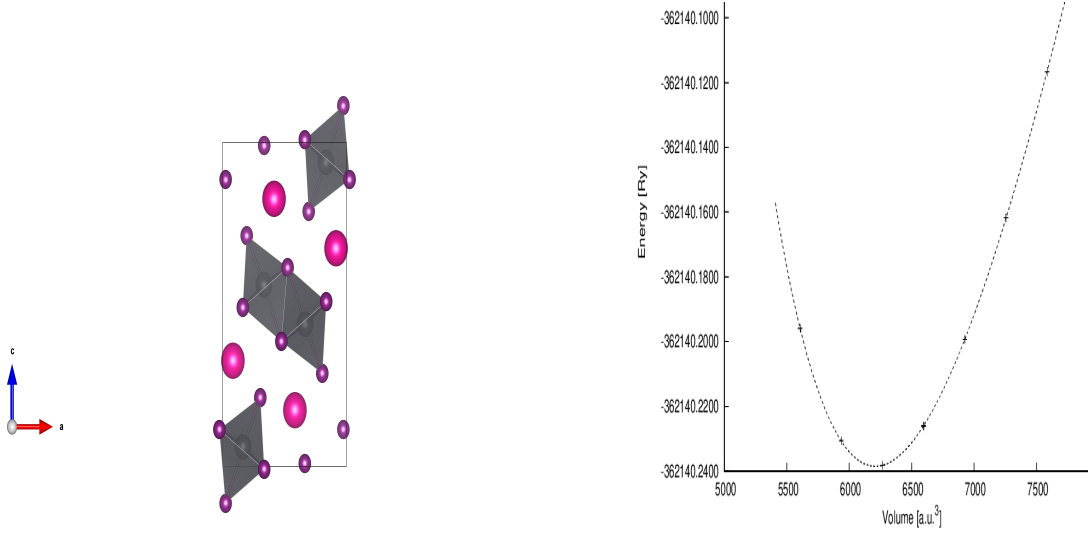


Figure 1: Left: Unit cell of RbPbX₃. Magenta, grey and purple spheres represent Rb, Pb and X atoms respectively; Right: Volume optimization for RbPbI₃.

Ernzerhof [23]. Structural unit for all the orthorhombic phases consists of 4 formula units. Values of RK_{\max} are set to 9, 8, 8 for RbPbCl₃, RbPbBr₃ and RbPbI₃ respectively, it determines the size of the basis sets in the calculation. Muffin tin radii have been selected in such a way, that it should not be large enough to leak charges from the sphere and small enough to increase the calculation time. The muffin tin radii are set to 2.5 a.u for all atoms in RbPbI₃, 2.31 a.u for all in RbPbBr₃; 2.5 a.u. are for Rb and Pb and 2.2 a.u. for Cl in the case of RbPbCl₃. Brillouin zone integrations are performed by the tetrahedron method, $6 \times 13 \times 3$, $6 \times 12 \times 3$ and $6 \times 13 \times 3$ k-mesh have been used for RbPbI₃, RbPbBr₃ and RbPbCl₃ respectively. But a denser k points of $13 \times 27 \times 7$ i.e. 392 in the irreducible BZ, are used to estimate the imaginary part of the dielectric tensor during the optical property estimation. Optical properties are calculated with OPTIC [24] as implemented in Wien2k. The energy and charge convergence criteria have been fixed as 0.0001 Ryd and 0.001e respectively. Structural lattice parameters are estimated by fitting energy and volume to the Murnaghan equation of state [25] for each compound.

3 Results and discussion

3.1 Electronic structure results

The estimated lattice parameters which are listed in Table 1, show good agreement with the experiments. From Table 1, it is observed that lattice constants decrease from RbPbI₃ to RbPbCl₃ as expected [26]. This is due to the decrease of atomic size of halides from I to Cl. The optimized volume of RbPbI₃ can be found from Fig 1. Optimized lattice parameters are calculated from these optimized volumes. The volume optimization graph for RbPbI₃ is shown only as it is similar for two other materials.

Density of states (DOS) and bandstructure will help to describe the electronic features of RbPbX₃ compounds. It is observed from the bandstructure that the valence band maximum (VBM) and the conduction band minimum (CBM) occurs at Γ and at X respectively, which implies that it is an indirect band gap semiconductor and is well agreed with the similar calculation [12]. As the band-diagrams are similar for all three structures, in the Fig 2 only the bandstructure of RbPbBr₃ has been shown. Partial density of states (PDOS) is given in the

	Present calculation			Experiment		
	a	b	c	a	b	c
RbPbI ₃	10.540	4.897	17.817	10.42	4.841	17.615
RbPbBr ₃	9.529	4.678	16.678	9.354	4.591	16.372
RbPbCl ₃	9.108	4.471	15.942	—	—	—

Table 1: Lattice parameters are in Angstrom for RbPbX₃, references for experimental parameters for RbPbI₃ and RbPbBr₃ are [20] and [21] respectively.

	Our calculation	Other calculation	experiment
RbPbI ₃	2.45	2.663[28]	2.64[12]
RbPbBr ₃	2.77	—	—
RbPbCl ₃	3.27	—	—

Table 2: The band gap values for RbPbX₃ are in eV

Figure 2. 6s, 6p orbits of Pb and p orbit of halide X make the contribution to the VBM while the major contribution comes from p orbit of X atoms. 6p of Pb and p orbit of halide atoms are responsible for the CBM but it is dominated by p orbit of Pb atoms. The lowest lying energy broad peak is centered at -7.5 eV and comes mainly from 6s orbital of Pb atom. The second lowest lying energy states which have range from 0 to -2.64 eV for RbPbI₃; 0 to -2.78 eV for RbPbBr₃ and 0 to -2.83 eV for RbPbCl₃ and these are contributed by p orbits of halide X, 6p of Pb and 6s of Pb but it is dominant by p orbits of halide atoms. Above the Fermi level, first broad peak ranges from 2.44 eV to 4.12 eV for RbPbI₃; 2.81 eV to 4.77 eV for RbPbBr₃ and 3.39 eV 5.29 eV for RbPbCl₃ structure. These states are occupied by the 6p orbit of Pb and p of X atoms. All peaks are shifted towards the higher energy as we move from RbPbI₃ to RbPbCl₃.

The calculated band gap values are 2.45, 2.77 and 3.27 eV corresponding to RbPbI₃, RbPbBr₃ and RbPbCl₃ respectively. The band gap increases from I to Cl in RbPbX₃ due to the decrease of the halide atomic radii. For the band gap calculation GGA underestimates in comparison with the experimental values. This happens because of the fact that the exchange-correlation term can not be handled accurately [27]. To the best of our knowledge the electronic structure of RbPbBr₃ of NH₄CdCl₃ type structure is calculated for the first time.

3.2 Optical properties

The optical properties of the halide perovskite materials have been studied theoretically from the complex dielectric function $\varepsilon(q, \omega)$, where q is the momentum due to the electron-phonon interaction and ω is then energy. The momentum transfer is assumed to be zero at lower energy and electric dipole approximation is considered for the optical analysis [29]. The complex dielectric function at lower energy is expressed by

$$\varepsilon(\omega) = \varepsilon_1(\omega) + i\varepsilon_2(\omega), \quad (1)$$

where $\varepsilon_1(\omega)$ and $\varepsilon_2(\omega)$ are the real and imaginary part of the dielectric function, respectively. There are two types of transitions i.e. intraband and interband, each can be further separated into direct and indirect transitions category. RbPbX₃ being semiconductor, the intraband contributions is neglected in our calculation. The indirect interband transition is also neglected

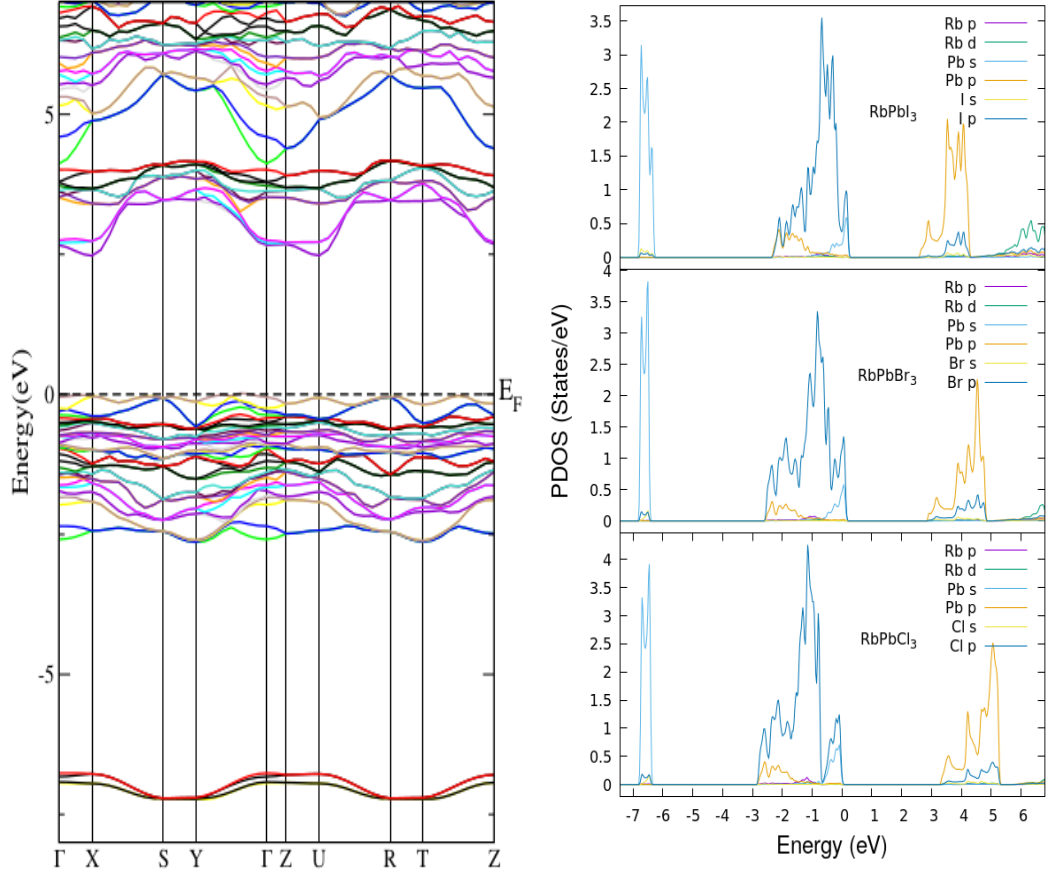


Figure 2: Left: bandstructure of RbPbBr₃; Right: PDOS for RbPbI₃, RbPbBr₃ and RbPbCl₃, Fermi level is set to 0 eV energy.

as it involves with the phonon scattering and its contribution is small [30]. For calculating the dielectric function, local field effect and finite lifetime effects have been ignored. The direct interband contribution to $\varepsilon_2(\omega)$ has been estimated by summing up all the transitions taken place between the occupied and unoccupied states. According to the dipole selection rules, momentum matrix elements allow or forbid interband transitions. Matrix elements are

$$M_G^{\text{ln}}(\mathbf{k}, \mathbf{q}) = \langle \psi_{\mathbf{k}-\mathbf{q}|\mathbf{l}} | e^{-i(\mathbf{q}+\mathbf{G})\mathbf{r}} | \psi_{\mathbf{k}\mathbf{n}} \rangle \quad (2)$$

A detailed description about the matrix is given in the following references [31, 32]. The off-diagonal terms of the dielectric tensor ε_2 are negligible compared to the diagonal elements due to the fact that principal axes make an orthogonal system. The diagonal elements of the tensor ε_2 is

$$\varepsilon_2^{ss} = \frac{8\pi^2 e^2}{m^2 \omega^2} \sum_n^{\text{unocc}} \sum_{n'}^{\text{occ}} \int_{BZ} |P_{nn'}^s(k)|^2 f_{kn}(1 - f_{kn'}) \times \delta(E_n^k - E_{n'}^k - \hbar\omega) \times \frac{d^3 k}{(2\pi)^3}, \quad (3)$$

where m and e are mass and charge of electrons, f_{kn} is the Fermi-Dirac distribution function, $P_{nn'}^s$ is the projection of the momentum matrix along s i.e. x, y, z directions and E_n^k is the single electron energy. Matrix elements are calculated over the muffin-tin as well as the interstitial regions. The total ε_2^{ss} has been estimated over the irreducible Brillouin zone (IBZ) as

$$\varepsilon_2^{ss} = \frac{1}{N} \sum_{i=1}^N \sigma_i^T \varepsilon_2(\text{IBZ}) \sigma_i, \quad (4)$$

where σ_i and N are the symmetry operations and the number of symmetry operations respectively. Using Kramer-Kronig relation, the real part of the dielectric tensor ε_1 can be estimated as

$$\varepsilon_1(\omega) = 1 + \frac{2}{\pi} \int_0^\infty \varepsilon_2(\omega') \omega' d\omega' / (\omega'^2 - \omega^2). \quad (5)$$

With the help of real and imaginary part of dielectric function, refractive index and extinction coefficient can be evaluated as follows

$$n(\omega) = \frac{1}{\sqrt{2}} [\sqrt{\varepsilon_1^2(\omega) + \varepsilon_2^2(\omega)} + \varepsilon_1(\omega)]^{1/2}, \quad (6)$$

$$k(\omega) = \frac{1}{\sqrt{2}} [\sqrt{\varepsilon_1^2(\omega) + \varepsilon_2^2(\omega)} - \varepsilon_1(\omega)]^{1/2}. \quad (7)$$

Further reflectivity (R) due to normal incidence, absorption coefficient (α) and ELF (L) can be expressed as a function of the extinction coefficient and refractive index using

$$R = \frac{(n - 1)^2 + k^2}{(n + 1)^2 + k^2}, \quad (8)$$

$$\alpha = \frac{2\omega k}{c}, \quad (9)$$

$$L = -\text{Im} \left(\frac{1}{\varepsilon_1 + i\varepsilon_2} \right) = \frac{\varepsilon_2}{\varepsilon_1^2 + \varepsilon_2^2}, \quad (10)$$

where ε_1 , ε_2 , n , k are used for $\varepsilon_1(\omega)$, $\varepsilon_2(\omega)$, $n(\omega)$, $k(\omega)$ respectively and c is the velocity of light in free space.

The large number of sub-bands are involved for the orthorhombic system compared to the cubic one. So, the interband transitions as well as peak positions for ε_2 spectra corresponding

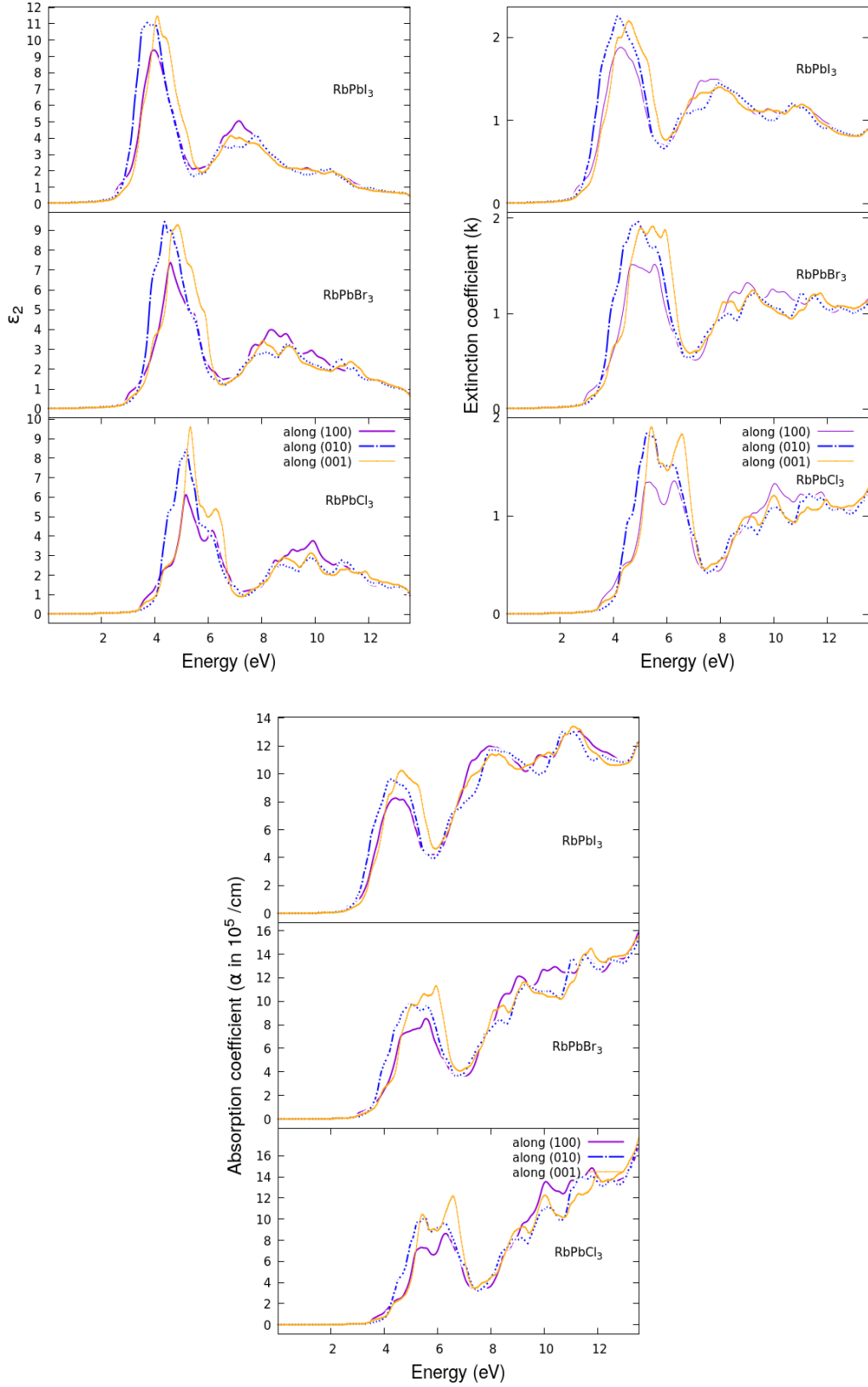


Figure 3: Top left: Imaginary part of the dielectric function ϵ_2 ; Top right: Extinction coefficient k ; Bottom: Absorption coefficient α as a function of photon energy for RbPbX₃ where X runs from I to Cl along the three polarization directions

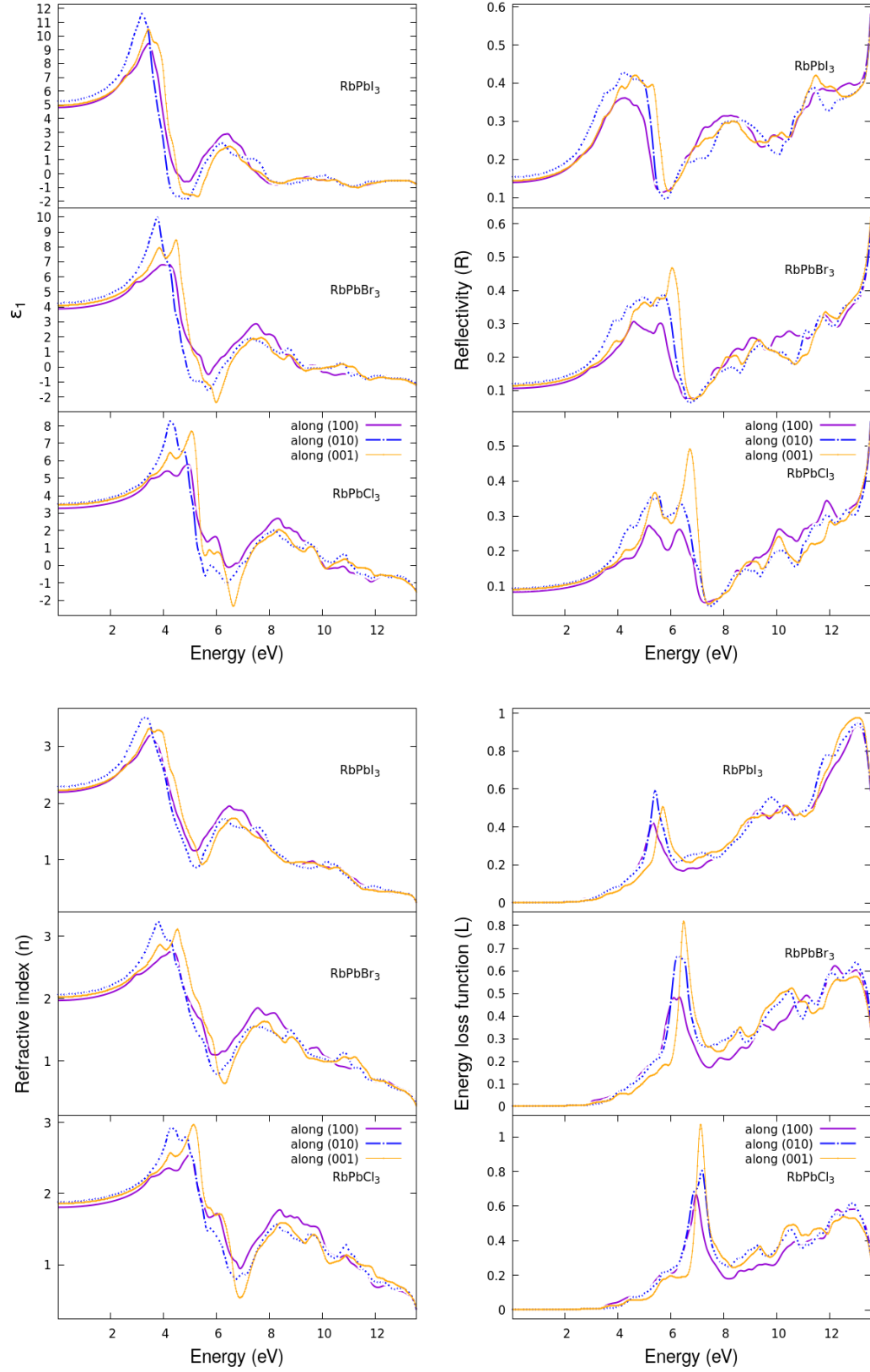


Figure 4: Top left: the real part of the dielectric function ϵ_1 ; Top right: Reflectivity R ; Bottom left: Refractive index n ; Bottom right: Energy loss function L for RbPbI₃, RbPbBr₃, RbPbCl₃

	RbPbI ₃			RbPbBr ₃			RbPbCl ₃		
Along	$\varepsilon_1(0)$	$R(0)$	$n(0)$	$\varepsilon_1(0)$	$R(0)$	$n(0)$	$\varepsilon_1(0)$	$R(0)$	$n(0)$
(100)	4.8135	0.140	2.194	3.877	0.107	1.969	3.275	0.091	1.810
(010)	5.248	0.154	2.290	4.262	0.121	2.064	3.545	0.094	1.883
(001)	4.953	0.144	2.226	4.093	0.115	2.023	3.464	0.083	1.861

Table 3: Static values for ε_1 , R , n for RbPbX₃ along different polarization directions.

to k of DOS are difficult to analyze. Therefore, we have preferred the analysis of the interband transitions corresponding to the main peaks of ε_2 for all the structures at the low energy region along the x , y , z polarization directions. It can be seen from the figure 3 that the nature of ε_2 is similar for all RbPbX₃ structures. It is observed from the Fig 2 that the VB width is narrower for RbPbI₃ as compared to RbPbBr₃ and RbPbCl₃. Moreover, RbPbI₃ displays higher peak intensity and smaller peak width in the ε_2 spectra. The spectra are also shifted towards the higher energy region as the halide is changed from I to Cl in RbPbX₃. It is due to the increase of the band gap from I to Cl. Projected density of states will predict states responsible for transitions corresponding to a particular peak in the spectra of ε_2 . Three peaks are observed. The first peak is due to the transition of electrons from a mixed states of (I,Br,Cl)-p, Pb-6s to 6p conduction state of Pb. The second and third peaks are observed due to the electronic transitions from (I,Br,Cl)-p valence states to Rb-4d unoccupied conduction states and Pb-6s to a mixed states of Pb-6p and (I,Br,Cl)-p states respectively. Similar kind of transitions have been observed for CsPbX₃ [26]. The spectrum are shifted towards the higher energy region as the halide changes from I to Cl. Extinction coefficient spectra also displays the similar behavior as ε_2 . It is observed from the Fig 3 that absorption coefficients have higher peaks for (001) polarization direction till 7 eV energy of the spectra for all structures. The reason is that the extinction coefficients along (001) directions have high peaks as along the (010) directions while peak positions are in the higher energy region for (001) direction.

The spectra of real part of the dielectric function have been shown in the figure 4. At frequency zero, the value of $\varepsilon_1(0)$ is the static dielectric constant. Fig 4 shows that $\varepsilon_1(0)$ decreases from RbPbI₃, RbPbBr₃ and then to RbPbCl₃. It proves the inverse relationship with the band gap. Similar feature has been observed for other materials [33, 34]. The calculated dielectric constants are matching well with the previous report [28] where values are 5.0, 4.4 and 4.3 along (001), (010) and (001) polarization directions respectively in the case of RbPbI₃. The dielectric constant value is closer to that of a compound having an active lone pair (5.64) and these Pb-halide based materials can be polarized to an external field [28]. ε_1 increases from zero photon energy, it attains maximum value and then decreases. At some frequency, it goes below zero, indicating the metallic behavior. The real part of the static dielectric constants $\varepsilon_1(0)$ decreases from I to Cl. All values are higher along (010) directions. Values of $\varepsilon_1(0)$, $n(0)$, $R(0)$ along (100), (010), (001) polarization directions are listed in Table 3. The reflectivity starts from 14%, 15.4% and 14.4% for RbPbI₃ along (100), (010), (001) directions respectively. While for RbPbBr₃ and RbPbCl₃ these values are 10.7%, 12% 11.5% and 8.3%, 9.3%, 9% respectively. Starting reflectivity decreases from I to Cl as reported in [26]. Sharp peaks in the energy loss function $L(\omega)$ spectra provide the plasma frequency. This frequency is the result of oscillations of electrons in valence states of the crystal. Peaks in $L(\omega)$ spectra are located at those energies corresponding to which, reflectivity R has minimum amplitudes as shown in the figure 4. The ELF is higher for RbPbCl₃ near 7 eV compared to that of RbPbBr₃ and RbPbI₃. It happens because of the fact that RbPbCl₃ has the lowest minimum near 7 eV for the spectra of ε_2 .

Crystallographic directions	RbPbI ₃		RbPbBr ₃		RbPbCl ₃	
	electron	hole	electron	hole	electron	hole
$\Gamma \rightarrow X$	0.245	0.098	0.128	0.112	0.511	0.095
$\Gamma \rightarrow S$	0.143	0.451	0.123	0.298	0.189	0.386
$X \rightarrow S$	0.026	0.152	0.030	0.180	0.037	0.386
$\Gamma \rightarrow Z$	0.119	0.030	0.056	0.029	0.056	0.035
$\Gamma \rightarrow U$	0.065	0.053	0.065	0.054	0.076	0.065
$Z \rightarrow U$	0.293	0.331	0.446	1.321	2.732	2.849

Table 4: The calculated effective masses of electrons and holes for RbPbX₃ along the high symmetric directions.

3.3 Transport properties

In order to find the transport behaviour of photo-generated electrons and holes, effective mass of electrons and holes are calculated along the high symmetry directions. The effective mass has been calculated by using the relation

$$\frac{1}{m_{\text{eff}}} = \frac{1}{\hbar^2} \frac{\partial^2 E}{\partial k^2}. \quad (11)$$

The effective masses for electrons and holes have been estimated by fitting the energy and k values corresponding to the lowest conduction band and the highest of the valence band obtained from the band-diagrams respectively. Estimated effective masses in terms of the free electron mass are represented in Table 4. The average effective masses of electrons and holes for RbPbI₃ are 0.1485 and 0.185 respectively. Average effective masses of electrons and holes for RbPbBr₃ and RbPbCl₃ are 0.141, 0.332; 0.600 and 0.636 respectively. RbPbI₃ has smallest effective masses for electrons and holes compared to other two structures which suggests highest mobility as well as longest diffusion lengths. For RbPbI₃ the effective mass of electron is smaller than that of hole. This proves that electrons can be transported easily than holes. Another study has also been reported that RbPbI₃ can transfer electrons to TiO₂ [28], because, the CBM of RbPbI₃ is higher than that of TiO₂. Because of the flat nature of the band diagram, the effective masses are higher compared to that of the hybrid lead halide perovskites.

4 Conclusion

In summary, we have explored the optoelectronic properties of orthorhombic rubidium lead halide (RbPbX₃, where X=I,Br,Cl) and compared various properties such as dielectric function, absorption coefficient, refractive index and transport properties with the help of first principle calculations. Electronic band structure calculations imply that these materials are wide band gap semiconductors with lowest band gap of 2.45 eV (for RbPbI₃). It is evident from the PDOS plot that the VBM of RbPbX₃ is dominantly occupied by p orbits of halide atoms while the CBM is populated by p orbits of Pb atoms. Calculated average dielectric constants (5.005, 4.077 and 3.428) and refractive indices (2.237, 2.019 and 1.851) decrease as the halide changes from I to Cl. Moreover, the static values of dielectric constants, reflectivity and refractive indices of all the RbPbX₃ display anisotropic behavior with maximum along [001] polarization direction. The effective masses of electron and hole are found to be minimum for RbPbBr₃ and RbPbI₃, indicating an efficient transport of electrons/ holes in the corresponding materials, respectively. The result from the first principle calculations indicate that among all three rubidium lead halide structures, RbPbI₃ is the most promising one for the photovoltaic applications due to

lower band gap energies. However, further study on the band gap tuning through suitable doping is required for its potential application in solar cells.

References

- [1] Woon Seok Yang, Byung-Wook Park, Eui Hyuk Jung, Nam Joong Jeon, Young Chan Kim, Dong Uk Lee, Seong Sik Shin, Jangwon Seo, Eun Kyu Kim, Jun Hong Noh, et al. Iodide management in formamidinium-lead-halide-based perovskite layers for efficient solar cells. *Science*, 356(6345):1376–1379, 2017.
- [2] Jangwon Seo, Jun Hong Noh, and Sang Il Seok. Rational strategies for efficient perovskite solar cells. *Accounts of chemical research*, 49(3):562–572, 2016.
- [3] Wiley A Dunlap-Shohl, Yuanyuan Zhou, Nitin P Padture, and David B Mitzi. Synthetic approaches for halide perovskite thin films. *Chemical reviews*, 119(5):3193–3295, 2018.
- [4] Xiangtong Meng, Xun Cui, Matthew Rager, Shuguang Zhang, Zewei Wang, Jiwoo Yu, Yeu Wei Harn, Zhitao Kang, Brent K Wagner, Yang Liu, et al. Cascade charge transfer enabled by incorporating edge-enriched graphene nanoribbons for mesostructured perovskite solar cells with enhanced performance. *Nano Energy*, 52:123–133, 2018.
- [5] Hua Dong, Jun Xi, Lijian Zuo, Jingrui Li, Yingguo Yang, Dongdong Wang, Yue Yu, Lin Ma, Chenxin Ran, Weiyin Gao, et al. Conjugated molecules “bridge”: Functional ligand toward highly efficient and long-term stable perovskite solar cell. *Advanced Functional Materials*, 29(17):1808119, 2019.
- [6] Samuel D Stranks, Victor M Burlakov, Tomas Leijtens, James M Ball, Alain Goriely, and Henry J Snaith. Recombination kinetics in organic-inorganic perovskites: excitons, free charge, and subgap states. *Physical Review Applied*, 2(3):034007, 2014.
- [7] Andrei Buin, Riccardo Comin, Jixian Xu, Alexander H Ip, and Edward H Sargent. Halide-dependent electronic structure of organolead perovskite materials. *Chemistry of Materials*, 27(12):4405–4412, 2015.
- [8] Ravi K Misra, Sigalit Aharon, Baili Li, Dmitri Mogilyansky, Iris Visoly-Fisher, Lioz Etgar, and Eugene A Katz. Temperature-and component-dependent degradation of perovskite photovoltaic materials under concentrated sunlight. *The journal of physical chemistry letters*, 6(3):326–330, 2015.
- [9] Heng-Yun Ye, Wei-Qiang Liao, Chun-Li Hu, Yi Zhang, Yu-Meng You, Jiang-Gao Mao, Peng-Fei Li, and Ren-Gen Xiong. Bandgap engineering of lead-halide perovskite-type ferroelectrics. *Advanced materials*, 28(13):2579–2586, 2016.
- [10] Giles E Eperon, Giuseppe M Paterno, Rebecca J Sutton, Andrea Zampetti, Amir Abbas Haghighirad, Franco Cacialli, and Henry J Snaith. Inorganic caesium lead iodide perovskite solar cells. *Journal of Materials Chemistry A*, 3(39):19688–19695, 2015.
- [11] Dong-Ho Kang and Nam-Gyu Park. On the current–voltage hysteresis in perovskite solar cells: Dependence on perovskite composition and methods to remove hysteresis. *Advanced Materials*, page 1805214, 2019.
- [12] Mi-Hee Jung, Sonny H Rhim, and Dohyun Moon. Tio₂/rbpb_i3 halide perovskite solar cells. *Solar Energy Materials and Solar Cells*, 172:44–54, 2017.

- [13] Jacob B Hoffman, A Lennart Schleper, and Prashant V Kamat. Transformation of sintered cspbbr3 nanocrystals to cubic csppi3 and gradient cspbbr x i3-x through halide exchange. *Journal of the American Chemical Society*, 138(27):8603–8611, 2016.
- [14] Michael Kulbak, David Cahen, and Gary Hodes. How important is the organic part of lead halide perovskite photovoltaic cells? efficient cspbbr3 cells. *The journal of physical chemistry letters*, 6(13):2452–2456, 2015.
- [15] Anton Kovalsky, Lili Wang, Gage T Marek, Clemens Burda, and Jeffrey S Dyck. Thermal conductivity of ch3nh3ppi3 and csppi3: Measuring the effect of the methylammonium ion on phonon scattering. *The Journal of Physical Chemistry C*, 121(6):3228–3233, 2017.
- [16] Youngho Kang and Seungwu Han. Intrinsic carrier mobility of cesium lead halide perovskites. *Physical Review Applied*, 10(4):044013, 2018.
- [17] In Chung, Jung-Hwan Song, Jino Im, John Androulakis, Christos D Malliakas, Hao Li, Arthur J Freeman, John T Kenney, and Mercouri G Kanatzidis. Csnpi3: semiconductor or metal? high electrical conductivity and strong near-infrared photoluminescence from a single material. high hole mobility and phase-transitions. *Journal of the American Chemical Society*, 134(20):8579–8587, 2012.
- [18] Michael Saliba, Taisuke Matsui, Konrad Domanski, Ji-Youn Seo, Amita Ummadisingu, Shaik M Zakeeruddin, Juan-Pablo Correa-Baena, Wolfgang R Tress, Antonio Abate, Anders Hagfeldt, et al. Incorporation of rubidium cations into perovskite solar cells improves photovoltaic performance. *Science*, 354(6309):206–209, 2016.
- [19] Un-Gi Jong, Chol-Jun Yu, Yun-Sim Kim, Yun-Hyok Kye, and Chol-Ho Kim. First-principles study on the material properties of the inorganic perovskite $\text{rb}_{1-x}\text{cs}_x\text{ppi}_3$ for solar cell applications. *Phys. Rev. B*, 98:125116, Sep 2018.
- [20] DM Trots and SV Myagkota. High-temperature structural evolution of caesium and rubidium triiodoplumbates. *Journal of Physics and Chemistry of Solids*, 69(10):2520–2526, 2008.
- [21] Matthew Ronald Linaburg. *Studies of Halide Perovskites CsPbX₃, RbPbX₃ (X= Cl-, Br-, I-), and Their Solid Solutions*. PhD thesis, The Ohio State University, 2015.
- [22] P Blaha, K Schwarz, GKH Madsen, D Kvasnicka, and J Luitz. Wien2k, an augmented plane wave plus local orbitals program for calculating crystal properties (vienna university of technology, austria, 2001). *There is no corresponding record for this reference.[Google Scholar]*, 2002.
- [23] John P Perdew, Kieron Burke, and Matthias Ernzerhof. Generalized gradient approximation made simple. *Physical review letters*, 77(18):3865, 1996.
- [24] Claudia Ambrosch-Draxl and Jorge O Sofo. Linear optical properties of solids within the full-potential linearized augmented planewave method. *Computer physics communications*, 175(1):1–14, 2006.
- [25] Francis Dominic Murnaghan. Finite deformations of an elastic solid. *American Journal of Mathematics*, 59(2):235–260, 1937.
- [26] G Murtaza and Iftikhar Ahmad. First principle study of the structural and optoelectronic properties of cubic perovskites cspbm3 (m= cl, br, i). *Physica B: Condensed Matter*, 406(17):3222–3229, 2011.

- [27] M Dadsetani and A Pourghazi. Optical properties of strontium monochalcogenides from first principles. *Physical Review B*, 73(19):195102, 2006.
- [28] Jakoah Brgoch, Anna J Lehner, Michael Chabinyc, and Ram Seshadri. Ab initio calculations of band gaps and absolute band positions of polymorphs of rbpbi3 and cspbi3: implications for main-group halide perovskite photovoltaics. *The Journal of Physical Chemistry C*, 118(48):27721–27727, 2014.
- [29] P. Ravindran, A. Delin, R. Ahuja, B. Johansson, S. Auluck, J. M. Wills, and O. Eriksson. Optical properties of monoclinic SnI_2 from relativistic first-principles theory. *Phys. Rev. B*, 56:6851–6861, Sep 1997.
- [30] S. Lebègue, B. Arnaud, and M. Alouani. Calculated quasiparticle and optical properties of orthorhombic and cubic Ca_2Si . *Phys. Rev. B*, 72:085103, Aug 2005.
- [31] M. Alouani and J. M. Wills. Calculated optical properties of si, ge, and gaas under hydrostatic pressure. *Phys. Rev. B*, 54:2480–2490, Jul 1996.
- [32] R. Ahuja, S. Auluck, J. M. Wills, M. Alouani, B. Johansson, and O. Eriksson. Optical properties of graphite from first-principles calculations. *Phys. Rev. B*, 55:4999–5005, Feb 1997.
- [33] B.Amin, Iftikhar Ahmad, M. Maqbool, S. Goumri-Said, and R. Ahmad. Ab initio study of the bandgap engineering of $\text{Al}_{1-x}\text{Ga}_x\text{N}$ for optoelectronic applications. *Journal of Applied Physics*, 109(2):023109, 2011.
- [34] Muhammad Maqbool, Bin Amin, and Iftikhar Ahmad. Bandgap investigations and the effect of the in and al concentration on the optical properties of $\text{In}_x\text{Al}_{1-x}\text{N}$. *J. Opt. Soc. Am. B*, 26(11):2181–2184, Nov 2009.